Research Article

Electrochemical Proton-Coupled Electron Transfer at a Metal−Semiconductor−Solution Interface

Kai Cui, Karl S. Westendorff, Yuriy Román-Leshkov, Yogesh Surendranath, and Sharon Hammes-Schiffer*

Cite This: https://doi.org/10.1021/acscatal.5c06789

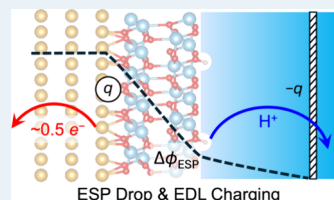Read Online

ACCESS | Metrics & More | Article Recommendations | Supporting Information

ABSTRACT: Interfacial proton-coupled electron transfer (I-PCET) in composite metal−semiconductor systems is important for many electrocatalytic processes. Herein, I-PCET at a metal−semiconductor−solution interface is investigated computationally using a Au-TiO$_2$ model system, where the proton transfers from the TiO$_2$ surface to an alcohol acceptor. We studied four possible I-PCET mechanisms that could occur in the system. For each mechanism, the calculated slope of the I-PCET equilibrium constant as a function of applied potential qualitatively agrees with experimental measurements of I-PCET-promoted Brønsted acid catalysis on a Ti-TiO$_2$ composite system, although the dependence of the calculated results on the thickness of the TiO$_2$ slab modeled prevents the unambiguous identification of the I-PCET mechanism. Focusing on one specific I-PCET mechanism, our charge analysis indicates that each proton transfer from the TiO$_2$ surface is coupled to the transfer of $n \approx 0.5$ electron from the Au metal to the external circuit. The calculated inverse slope of $\sim$110 mV is consistent with the Nernstian slope of a 1H$^+$-ne^- PCET process. Further analysis shows that the observed slope arises from both electrostatic and capacitive contributions from the interface, together leading to a $\sim$0.6 eV change in the reaction free energy for deprotonation per 1 V potential change. These analyses reveal distinctive I-PCET reaction characteristics at electrified metal−semiconductor−solution interfaces and provide fundamental insights into how catalyst material properties influence the potential dependence of these elementary steps.

KEYWORDS: *proton-coupled electron transfer, interface, electrochemistry, Brønsted acid catalyst, grand canonical, density functional theory, metal−semiconductor−solution*

INTRODUCTION

The chemical reactivity and catalytic properties of a solid-solution interface are strongly influenced by the local electrostatic potential and corresponding electric field experienced by the reacting molecules at the surface. This phenomenon has been widely exploited to drive electro-catalysis of redox half-reactions that involve the net transfer of charge (i.e., Faradaic current flow) across the interface.[1−7] However, these strong interfacial electric fields also have a large impact on redox neutral non-Faradaic reactions if one or more of the rate-controlling steps involves charge transfer across the interface.

Recently, the Román and Surendranath groups have experimentally demonstrated a strong enhancement of non-Faradaic Brønsted acid catalyzed alcohol dehydration and Friedel−Crafts acylation reactions upon polarization of a catalyst-solution interface to introduce an oriented and tunable electric field.[8] These experiments used either carbon-supported phosphotungstic acid (PTA/C) or Ti foils with passivating TiO$_2$ layers (Ti/TiO$_y$H$_x$) as the catalysts. Increasing the applied potential by $\sim$ 380 mV led to a 100,000-fold rate enhancement for 1-methylcyclopentanol dehydration catalyzed by PTA/C. This enhancement arises from the alteration of a pre-equilibrium proton transfer (PT) from one of the PTA sites on the polarized carbon interface to the 1-methylcyclo-

pentanol occurring prior to the rate-determining step (RDS).[8] As the electrochemical potential of the catalyst is increased, this interfacial PT step becomes more thermodynamically favorable. Since this interfacial PT reaction is charge-compensated by electron transfer (ET) to the external circuit and/or electron redistribution in the solid, this elementary step is a net interfacial proton-coupled electron transfer (I-PCET) reaction. In the dehydration reaction studied, this I-PCET step was found to be quasi-equilibrated and in minor equilibrium (i.e., reactants dominating over the products, $K_{I-PCET}(E) \ll 1$). Thus, the apparent rate constant of the overall reaction is proportional to the potential-dependent I-PCET equilibrium constant, $K_{I-PCET}(E)$ (Figure 1), engendering a potential dependence to the overall reaction.

The experimentally measured logarithm of the lower-bound turnover frequency (l.b. TOF) shows a linear correlation with the applied potential.[8] For the alcohol dehydration reaction, the slope was a decade change in TOF per 68 mV for the
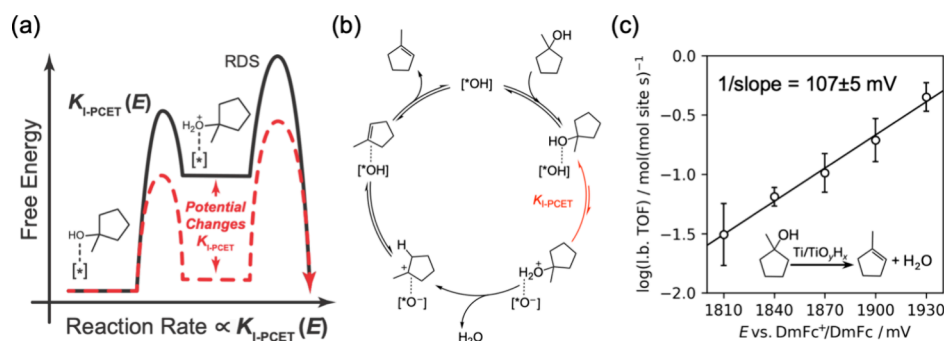
Figure 1. (a) Schematic of the potential-dependent I-PCET step, corresponding to the equilibrium constant $K_{I\text{-PCET}}$ (E), and its influence on the rate of 1-methylcyclopentanol dehydration. In this sequence, the surface-bound alcohol is in abundance relative to the surface-oxonium intermediate ($K_{I\text{-PCET}}$ $(E) \ll 1$ and is in minor equilibrium), and I-PCET occurs prior to the rate-determining step (RDS), thereby making the overall rate of the reaction proportional to the value of $K_{I\text{-PCET}}$ (E). (b) Proposed catalytic cycle for Brønsted acid catalyzed dehydration of 1-methylcyclopentanol. [*OH] represents the protonated catalyst, and [*O$^-$] represents the deprotonated catalyst. The I-PCET step is highlighted in red. (c) Experimentally measured potential-dependent lower-bound turnover frequency (l.b. TOF) of the Ti/TiO$_y$H$_x$ catalyzed alcohol dehydration reaction, replotted using the data from ref. 8. Figure inspired from ref. 8. Copyright 2024 American Association for the Advancement of Science.

PTA/C catalyst. This value is close to the Nernstian scaling for a $1H^+$-$1e^-$ PCET process, which corresponds to a decade change per 62 mV at the experimental temperature. However, the influence of polarization is attenuated for the same reaction on the Ti/TiO$_y$H$_x$ catalyst, where the measured rate-potential scaling becomes one decade change in TOF per 107 mV. Currently, the mechanistic basis for these different slopes is unclear. Because reaction kinetics were measured under similar reaction conditions and over identical kinetic regimes for both catalysts, this observation suggests that differences in rate-potential scaling may arise from differing catalyst material properties. Specifically, we hypothesize that the dielectric TiO$_2$ layer that separates the metallic Ti from the surface-exposed TiO$_y$H$_x$ active sites screens charge from the bulk metal, creating an electrostatic potential drop between the conductive interface and the active site, which is not present in PTA/C.

Computational models for heterogeneous electrochemical PCET involving only a metal electrode have been investigated extensively.[9−18] However, modeling the PCET reaction for a metal−semiconductor−solution system with two interfaces is more complicated, as the electronic structure of the heterostructure can be significantly affected by the band bending[19−22] and charge redistribution[23,24] at both interfaces, as well as the formation of metal-induced gap states.[23−25] Additionally, the defects within the semiconductor need to be considered.[26−30] For a PCET reaction at a semiconductor surface, PT to or from the surface coincides with ET involving small polaronic defects in the semiconductor, where an excess electron or hole is accompanied by local bond distortions.[31−34] Polaronic defects and their influence on the PCET reaction at a TiO$_2$ surface have been characterized computationally.[33,34] Two types of defects, d-band electrons and valence p-band holes, may exist in TiO$_2$. The former corresponds to a filled electronic state that lies in the band gap, whereas the latter corresponds to an unoccupied state in the band gap (Figures S4 and S5 in ref 33). The bond dissociation free energies (BDFEs) of the O−H bonds associated with these two types of defects were shown computationally to differ by ~ 3.50 eV, indicating a significant influence on PCET thermodynamics by such defects.[33] Despite this understanding, it remains unclear if polaronic defects participate in the I-PCET process on the Ti/TiO$_y$H$_x$ catalyst and affect the potential scaling.

In this paper, we perform first-principles calculations to investigate the electronic structure and the potential dependence of the I-PCET reaction at a metal−semiconductor−solution interface. Using a model Au-TiO$_2$ system, we elucidate the mechanism of proton transfer and the associated charge redistribution at the semiconductor−solution interface. We show that the attenuated potential response observed experimentally in metal−semiconductor systems arises from both the internal electrostatic potential drop across the TiO$_2$ slab and the differences in the capacitive contributions of the protonated and deprotonated surfaces. This work provides a microscopic basis for understanding PCET reactivity at heterogeneous interfaces involving semiconducting components.

■ COMPUTATIONAL METHODS

We used periodic density functional theory (DFT) at the PBE+U level[35,36] to compute the electronic structure of the metal-TiO$_2$ heterostructure with the Quantum ESPRESSO[37,38] software package. It is well-known that generalized gradient approximation (GGA) functionals such as the PBE functional can significantly underestimate the band gap of metal oxides.[39,40] Although hybrid functionals provide a better descriptions of the TiO$_2$ slab, they are less accurate for metallic systems.[41,42] On the other hand, previous studies have shown that with a reasonable choice of the U parameter, the PBE+U method can produce the correct band gap for TiO$_2$.[43,44] Thus, the PBE+U method provides a practical and sufficiently accurate description of the system for this study. The metal-TiO$_2$ heterostructure is modeled as stacked metal and TiO$_2$ slabs, with three layers of metal and two or three layers of anatase TiO$_2$ (101), as illustrated in Figure 2. The atomic positions in the metal and TiO$_2$ slabs were optimized separately in vacuum before stacking, and the distance between the slabs was determined by a rigid scan (Figure S1). In our test calculations, we found unphysical spin segregation in the spin-polarized calculations on a Ti slab, which is due to insufficient Brillouin zone sampling. Solving this issue for Ti requires a much denser k-point mesh, which is not computationally affordable for this large composite system. Therefore, we used the Au(111) surface as a prototypical model for the metal electrode. The distance between neighboring Au atoms within a layer of the metal slab is 2.66 Å. Additional computational details are provided in the Supporting Information.

We calculated the thermodynamics of I-PCET reactions on the Au-TiO$_2$ surface with a constant electrode potential using a capacitor model developed previously[45] and inspired by earlier works.[46−49] In
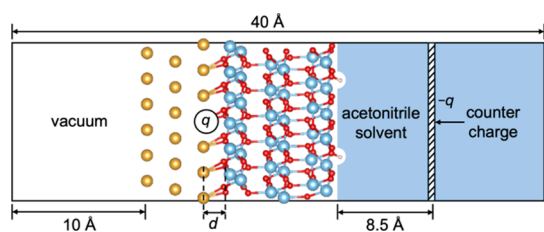
Figure 2. Schematic illustration of the computational unit cell of the model Au-TiO$_2$ system with three layers of TiO$_2$, corresponding to a total thickness of 11 Å for the TiO$_2$ slab. The projected density of states (PDOS) calculations were performed on a neutral slab ($q = 0$) in vacuum, whereas the grand potential calculations were performed on charged slabs in implicit solvent. The proton acceptor, 1-methylcyclopentanol (ROH), in bulk acetonitrile solvent was modeled as a separate system without periodic boundary conditions. A strip of counter charge was placed in the solvent to qualitatively model the EDL and ensure a neutral system.

this model, constant potential calculations are formulated in the grand canonical ensemble. The thermodynamic properties are described by the grand potential Ω, which is the Legendre transform of the Gibbs free energy, G:[50−52]

$$\Omega(E) = G(q) - \sum_i N_i \tilde{\mu}_i \qquad (1)$$

where E is the electrode potential and q is the total charge of the atomistic system. In this work, we model both the surface, which is the proton donor, and the proton acceptor, denoted as ROH, explicitly. In this context, N_i and $\tilde{\mu}_i$ are the particle number and electrochemical potential of the electrons. Thus, the grand potential can be expressed as[45]

$$\Omega(E) = G(q) - G_{ref} - \left(N_{H^+} - \frac{q}{e}\right)\tilde{\mu}_{e^-} \qquad (2)$$

where G_{ref} is the Gibbs free energy of a reference system. For I-PCET on the Au-TiO$_2$ surface, the reference system is the charge-neutral Au-TiO$_2$ slab and a protonated substrate ROH$_2^+$, which simply shifts all the grand potentials by the same constant. Moreover, N_{H^+} is the

number of protons transferred to the acceptor, and $N_{e^-} = N_{H^+} - q/e$ is the number of electrons added to the system.

The electrochemical potential for electrons is given by[53]

$$\tilde{\mu}_{e^-} = -eE \qquad (3)$$

where e is the elementary charge. In practice, we calculate the Gibbs free energy of both the protonated and deprotonated Au-TiO$_2$ systems (with or without polaronic defects) with various system charges q. The surface charge q in the atomistic system is balanced by a counter-charge layer of width 1.0 Å located $\sim$ 10 Å away from the surface in bulk solvent to simulate the electric double layer (EDL) and ensure charge neutrality of the simulation box (Figure 2). The proton acceptor, ROH in bulk acetonitrile solvent, is modeled as a separate system without periodic boundary conditions. The free energies of the protonated or deprotonated proton acceptor were added to the free energies of the deprotonated or protonated Au-TiO$_2$ surfaces, respectively, to obtain $G(q)$. For a given charge, the electrode potential can be calculated from the difference between the electrostatic potential (ESP) in bulk solvent and the Fermi energy of the surface. The grand potentials $\Omega(E)$ can be calculated using eq 2 for both the protonated and deprotonated Au-TiO$_2$ systems with or without polaronic defects.

We performed grand potential calculations on three different models for the Au-TiO$_2$-solution system at 298 K. In the first model, two layers of anatase TiO$_2$ (101) are stacked on the Au slab. The counter-charge layer is placed 12.5 Å from the top TiO$_2$ layer. This model is denoted as "2L". In the second and third models, three layers of TiO$_2$ are stacked on the Au slab. The counter-charge layers in these models are placed 8.5 Å or 12.5 Å from the top TiO$_2$ layer, denoted as "3L-1" (Figure 2) and "3L-2", respectively. In all these models, the dielectric constant of acetonitrile solvent near the surface is assumed to be the same as in bulk solvent. The influence of a low-dielectric region near the TiO$_2$ surface has also been tested on the 2L model (see Supporting Information).
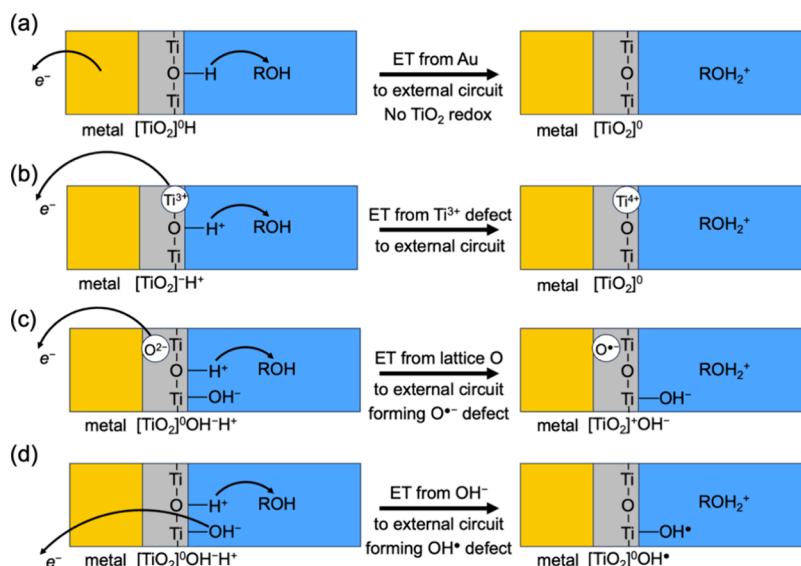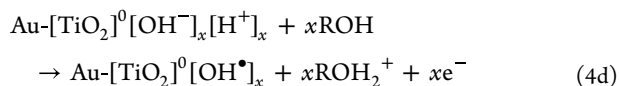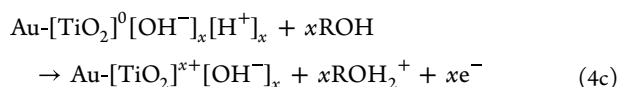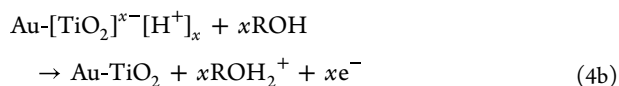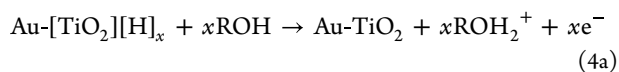

Figure 3. Schematic illustration of four possible I-PCET processes with PT from the surface of a metal-TiO$_2$ heterostructure to a proton acceptor, 1-methylcyclopentanol (ROH), in acetonitrile. For the reactant in (b) we choose a 6-coordinated Ti^{3+} ion (Ti$_{6c}^{3+}$) as the d-band defect. For the product in (c) we choose a 2-coordinated oxyl radical (O$_{2c}^{\bullet-}$) that is not the deprotonation site as the p-band defect. In part (d), we remove the proton from the bridge O atom rather than from the terminal OH group to be consistent with the site of deprotonation for parts (a-c). These choices were found to yield the most stable defect structures for each case at the level of theory used in this work.

■ RESULTS AND DISCUSSION

Possible I-PCET Processes at a Metal−Semiconductor−Solution Interface

To understand the mechanism of charge transfer during the I-PCET step at the metal−semiconductor heterostructure, we considered four possible charge transfer processes that may couple with PT from the surface, as shown in Figure 3. In the first process, PT from the TiO_yH_x surface to the proton acceptor is coupled with ET from the metal to the external circuit (Figure 3a). In this case, no redox event occurs in the TiO_2 layer, which therefore only serves as a proton donor. We then considered PT from the surface coupled with the oxidation of a d-band defect, where an electron is transferred from the TiO_2 layer to the external circuit, and the Ti^{3+} ion in the defect is oxidized to Ti^{4+} (Figure 3b). For the last two processes, we considered PT from the surface coupled with the oxidation of a lattice O^{2-} ion or a surface-adsorbed OH^- ion, leading to the formation of a p-band defect in the form of an oxyl radical $O^{\bullet-}$ in the lattice or a hydroxyl radical $OH^\bullet$ on the surface (Figure 3c,d, respectively). The balanced chemical reactions for all four processes are

$$Au\text{-}[TiO_2][H]_x + xROH \rightarrow Au\text{-}TiO_2 + xROH_2^+ + xe^- \tag{4a}$$

$$Au\text{-}[TiO_2]^{x-}[H^+]_x + xROH$$
$$\rightarrow Au\text{-}TiO_2 + xROH_2^+ + xe^- \tag{4b}$$

$$Au\text{-}[TiO_2]^0[OH^-]_x[H^+]_x + xROH$$
$$\rightarrow Au\text{-}[TiO_2]^{x+}[OH^-]_x + xROH_2^+ + xe^- \tag{4c}$$

$$Au\text{-}[TiO_2]^0[OH^-]_x[H^+]_x + xROH$$
$$\rightarrow Au\text{-}[TiO_2]^0[OH^\bullet]_x + xROH_2^+ + xe^- \tag{4d}$$

In our simulations, $x = 0.0278$ when the 2L model is used and 0.0185 when the 3L models are used. For notational simplicity, we will omit the x for the remainder of this paper. For example, $Au\text{-}[TiO_2]^{x-}[H^+]_x$ will be denoted as $Au\text{-}[TiO_2]^-H^+$.

Electronic Structure of the Composite System at Potential of Zero Free Charge

We first aimed to understand how the introduction of the underlying Au slab and its distance from the TiO_2 slab influences the electronic structure of the TiO_2 slab in our composite metal−semiconductor system at the potential of zero free charge (PZFC). We therefore calculated the projected density of states (PDOS) of the composite Au-TiO_2 system at various values of the interslab separation d in vacuum in Figure 4a. This separation d is defined as the distance between the averaged z coordinate of the top Au layer in the Au slab and the averaged z coordinate of the bottom O layer in the TiO_2 slab (Figure 2). When the Au and TiO_2 slabs move toward each other, the valence and conduction bands of TiO_2 shift slightly toward lower energy, as indicated by the decrease of the conduction band minimum (CBM) and valence band maximum (VBM) energies relative to the Fermi level when the interslab distance decreases from $d = 4$ Å to $d = 3$ Å. This shift may be interpreted as band bending, which is due to the redistribution of electrons between the two materials to equalize their Fermi levels upon contact.[21,23,24] We also observe the emergence of TiO_2 states within its band
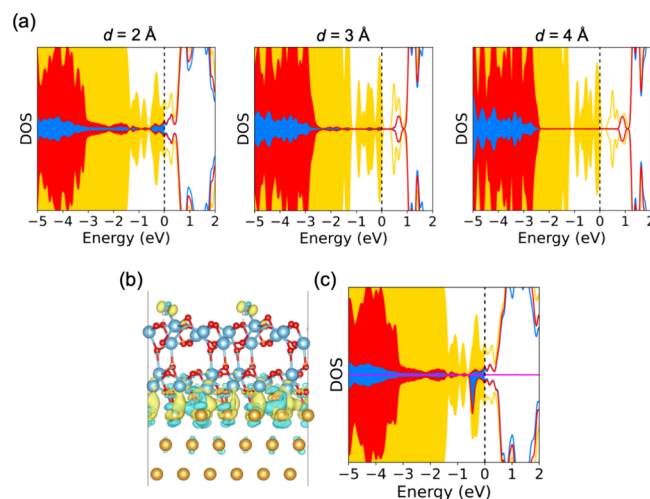

Figure 4. (a) PDOS of the composite Au-TiO_2 system at various interslab separations in vacuum. The PDOS for Ti, O, and Au are shown in blue, red, and gold, respectively. All energies are relative to the Fermi level. At the shorter Au-TiO_2 separations, metal-induced gap states (MIGS) appear in the TiO_2 band gap. This behavior is common at the interface of a semiconductor with a metal, where orbital hybridization leads to "partial metallization" within the semiconductor bandgap.[23−25] (b) Electron density difference plot $\Delta\rho = \rho_{Au\text{-}TiO_2} - \rho_{Au} - \rho_{TiO_2}$ of the Au-$[TiO_2]^0OH^\bullet$ composite system with $OH^\bullet$ p-band defects. Yellow represents positive $\Delta\rho$, indicating more electrons than in the isolated metal and TiO_2 systems. Cyan represents negative $\Delta\rho$, indicating fewer electrons in the composite system than in the isolated systems. The predominantly yellow surfaces on the $OH^\bullet$ p-band defects are indicative of ET from Au to these defects. The isosurface is set to be 0.004 Å^{-3}. (c) PDOS of the composite Au-$[TiO_2]^-H^+$ system with a Ti_{6c}^{3+} d-band defect. The color scheme is the same as in (a) with H shown in pink, although the PDOS for H is invisible due to the small number of states. All energies are relative to the Fermi level. The d-band defect appears as a blue peak slightly below the Fermi level.

gap upon contact with gold. These metal-induced gap states (MIGS) originate from the hybridization of the states at the interface and result in metal-like behavior of the semiconductor at the interface.[23−25] These MIGS were also observed for the Ti-TiO_2 system (Figure S2) at the equilibrium Ti-TiO_2 distance of 2 Å, indicating that the formation of MIGS is not an artifact due to the replacement of Ti by Au but rather is a property of the composite system. The equilibrium distance of 2 Å between the metal and TiO_2 slabs determined in the Ti-TiO_2 system will be used for the simulation of the Au-TiO_2 model system. At this distance, the band bending is noticeable, and the MIGS formation is significant.

We then investigated how the defect states in the TiO_2 slab are affected upon contact with Au. In the Au-TiO_2 system with a 2 Å interslab separation, the Fermi level of the composite system is higher than the energy levels of both types of p-band polaronic defects in TiO_2 (Figure 3c,d). In this case, the unoccupied p-band polaronic defects cannot exist in the composite system at PZFC due to spontaneous ET from Au to the defect state. The electron density difference plot of $\Delta\rho = \rho_{Au\text{-}TiO_2} - \rho_{Au} - \rho_{TiO_2}$ for the Au-$[TiO_2]^0OH^\bullet$ composite system with an $OH^\bullet$ defect clearly shows ET to the p-band defect when forming the composite system (Figure 4b). Similar behavior is observed for the $O^{\bullet-}$ defect. In terms of the

d-band defect, Figure 4c shows the PDOS of the Au-$[TiO_2]^-H^+$ composite system with a Ti_{6c}^{3+} (6-coordinated Ti^{3+} ion) defect. This defect lies below the Fermi level and remains occupied in the composite system at the PZFC.

At potentials away from PZFC, the presence of these defect states is dependent on their energies relative to the Fermi level of the electrode. Both the defect energy and the Fermi level change with the applied potential. Specifically, the Fermi level decreases monotonically as the applied potential becomes more positive. When the Fermi level is below the energy of the d-band defect (or equivalently, when the electrode potential is more positive than the redox potential of the d-band defect), this defect state is oxidized and no longer exists. As the electrode potential becomes more positive than the redox potential of the p-band defect, spontaneous ET from Au to the p-band defects does not occur, and such defects are present. We note that since the filling or unfilling of these defect states are all I-PCET processes, the overall free energy change of the system will still correlate strongly, though not necessarily Nernstianly (see below), with changes in the Fermi level.

Grand Potential Calculations

The contribution of each I-PCET reaction depicted in Figure 3 to the experimentally observed rate-potential scaling is predominately based on their respective redox potentials relative to the electrode potential. To determine each of these redox potentials, we performed grand potential calculations on the composite system for each I-PCET process in Figure 3 and calculated the grand potential difference between the product and reactant as a function of the electrode potential E. Figure 5a shows the calculated grand potential $\Omega(E)$ for the I-PCET process depicted in Figure 3a using the 2L model. For both the reactant (Au-TiO_2-H + ROH) and the product (Au-TiO_2 +
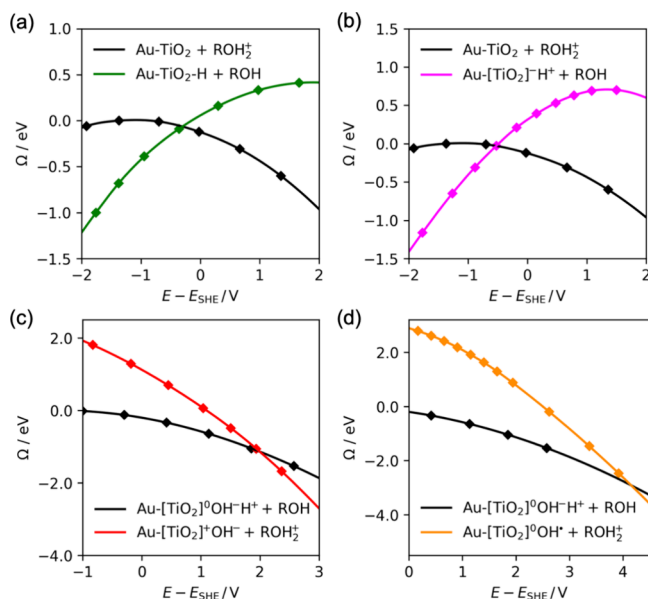
ROH_2^+), the grand potentials show nearly quadratic dependence on the electrode potential. This behavior is expected because the EDL is modeled as a charged capacitor, and the energy of an ideal capacitor depends quadratically on the potential.[45,46,54,55] The crossing point of the reactant and product $\Omega(E)$ curves gives the proton-coupled redox potential $E_{\text{I-PCET}}$ for the system. In the 2L model, the reactant and product $\Omega(E)$ curves intersect at −0.30 V vs SHE (+0.15 V vs DmFc$^+$/DmFc, DmFc = decamethylferrocene) in acetonitrile.

Using the same model, we then calculated the redox potentials for the I-PCET processes involving defects in Figure 3. We find that the proton-coupled redox potential for the I-PCET reaction involving a d-band defect (Figure 3b) is −0.55 V vs SHE in acetonitrile (Figure 5b), whereas the proton-coupled redox potentials for the I-PCET reaction involving p-band defects are +1.96 V and +4.16 V vs SHE in acetonitrile for the scenarios shown in Figure 3c,d, respectively (Figure 5c,d).

To understand how the thickness of the TiO_2 slab in the model influences our calculated redox potentials, we employed the 3L-1 model and calculated the redox potentials for each I-PCET process in Figure 3. We find that the $E_{\text{I-PCET}}$ for the process in Figure 3a using this model is +0.18 V vs SHE, which is 0.48 V more positive than the value obtained with the 2L model. The $E_{\text{I-PCET}}$ values for the defect I-PCET processes in Figure 3b–d all shift notably by +0.25, −0.83, and −0.61 V, respectively. These results indicate that the thickness of the TiO_2 slab used in the model can have a large impact on the calculated $E_{\text{I-PCET}}$. The alignment of the $E_{\text{I-PCET}}$ values for each I-PCET process using both the 2L and 3L-1 models with the experimentally relevant potential range[8,56,57] is shown in Figure 6.
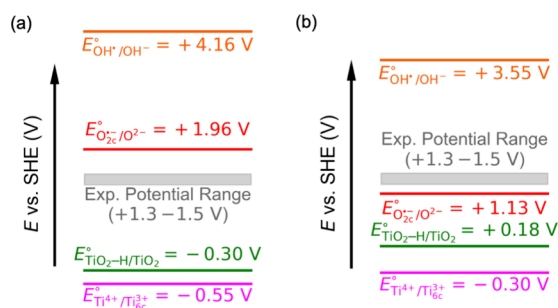

Figure 6. Alignment of the proton-coupled redox potentials of each I-PCET mechanism calculated using the (a) 2L and (b) 3L-1 models and the experimentally relevant potential range for the catalytic reaction. The green, pink, red, and orange lines correspond to each I-PCET process depicted in Figure 3a–d, respectively.

Figure 5. Calculated grand potential $\Omega(E)$ for (a) Au-TiO_2 + ROH_2^+ and Au-TiO_2-H + ROH, (b) Au-TiO_2 + ROH_2^+ and Au-$[TiO_2]^-H^+$ + ROH, (c) Au-$[TiO_2]^+OH^-$ + ROH_2^+ and Au-$[TiO_2]^0OH^-H^+$ + ROH, and (d) Au-$[TiO_2]^0OH^\bullet$ + ROH_2^+ and Au-$[TiO_2]^0OH^-H^+$ + ROH using the 2L model, corresponding to each process depicted in Figure 3a–d, respectively. The calculated data points are shown as filled diamonds, and the spline fits of the data are shown as solid lines. These calculations were performed at 298 K.

The grand potential data provide insight into the contributions of each I-PCET process to the observed rate-potential scaling. For the I-PCET processes in Figure 3a,b, both 2L and 3L-1 models show that over the experimentally relevant potential range (1.8−2.0 V vs DmFc$^+$/DmFc, corresponding to 1.3−1.5 V vs SHE in acetonitrile), the deprotonated Au-TiO_2 surface is more stable, indicating that PT from the surface to 1-methylcyclopentanol is thermodynamically favorable ($K_{\text{I-PCET}}(E) \gg 1$) in this potential range. In contrast, for the I-PCET process associated with the p-band defect in Figure 3d, the protonated Au-$[TiO_2]^0OH^-H^+$ surface is more stable ($K_{\text{I-PCET}}(E) \ll 1$) over the experimentally relevant potential range, whereas for the I-PCET process in

Figure 3c, $K_{\text{I-PCET}}(E) \ll 1$ using the 2L model but $K_{\text{I-PCET}}(E) \gg 1$ using the 3L-1 model. Based on the experimental observation that $K_{\text{I-PCET}}(E) \ll 1$, these data in isolation suggest that the I-PCET processes in Figure 3d may be responsible for the observed rate-potential scaling over the experimental potential range. However, we note that since the calculated $E_{\text{I-PCET}}$ values change significantly as the thickness of the TiO₂ slab used in the model composite system increases, the processes depicted in Figure 3a−c may also be experimentally relevant. Specifically, TiO₂ passivation layers in the experimental system (∼2−7 nm) are much thicker than the TiO₂ slabs used in the 2L and 3L-1 models (0.7 or 1.1 nm, respectively). Moreover, the use of a Au slab instead of a Ti slab in our calculations limits the quantitative accuracy of our calculated $E_{\text{I-PCET}}$ values.

Despite these factors influencing the calculated $E_{\text{I-PCET}}$ values, we proceeded to explore whether the $\log K_{\text{I-PCET}}$ scaling with E could provide additional insight into which I-PCET process is experimentally relevant. Using the calculated grand potential differences between the product and reactants, $\Delta\Omega(E) = \Omega_{\text{P}}(E) - \Omega_{\text{R}}(E)$, as a function of the electrode potential E for each process in Figure 3 with the 2L model, we plotted $\log K_{\text{I-PCET}}$ $(= -\Delta\Omega/2.303 k_{\text{B}}T)$ vs E to obtain this scaling. As shown in Figure 7, all four I-PCET processes

Table 1. Slopes of $\log K_{\text{I-PCET}}$ vs. the Electrode Potential Calculated Using the 2L and 3L-1 Models for the Four I-PCET Mechanisms in Figure 3

I-PCET mechanism	1/slope (mV)[a]	
	2L	3L-1
Au-TiO₂-H + ROH →Au-TiO₂ + ROH₂⁺ + e^- (case a)	98	108
Au-[TiO₂]⁻-H⁺ + ROH → Au-TiO₂ + ROH₂⁺ + e^- (case b)	125	171
Au-[TiO₂]⁰OH-H⁺ + ROH → Au-[TiO₂]⁺OH⁻ + ROH₂⁺ + e^- (case c)	88	66
Au-[TiO₂]⁰OH⁻H⁺ + ROH → Au-[TiO₂]⁰OH• + ROH₂⁺ + e^- (case d)	85	67

[a]Obtained directly from the potential-dependent grand potential calculations at 298 K shown in Figure 5 and Figure S4.

the TiO₂ slab (Table 1). Although the $\log K_{\text{I-PCET}}$-potential scaling of the I-PCET process in Figure 3a is most consistent with the experimentally observed value, these data do not unambiguously indicate the experimentally relevant I-PCET mechanism due to limitations of the model, such as the thickness of the slabs and the use of Au rather than Ti for the metal slab. Nevertheless, all these calculations agree qualitatively with the experimental observation.

Altogether, these calculations highlight the complexities associated with determining the kinetically relevant I-PCET processes at these interfaces. We stress that other factors, such as the relative populations of these I-PCET sites as well as their true distances from the underlying conductive metallic layer, also dictate their kinetic relevance. For the remainder of this work, we choose the I-PCET process in Figure 3a as an example case and decompose its E dependence into electrostatic and capacitive components.

Analysis of factors Influencing Potential Dependence of Equilibrium Constant

The attenuated potential dependence of I-PCET equilibrium constants near an electrode surface measured here has also been observed in other systems. An illustrative example is the potential-dependent deprotonation of 4-mercaptobenzoic acid (4-MBA) in an immobilized self-assembled monolayer (SAM) on a Au electrode.[58] In this study, the pK_{a} of 4-MBA in the SAM was found to depend linearly on the applied potential, with a slope of −0.1 pK_{a} unit per 59 mV increase in the electrode potential. The origin of this weak potential dependence was analyzed by viewing the deprotonation step as either an I-PCET reaction or a pure PT reaction in an external electric field. When considered as an I-PCET reaction, this weak potential dependence can be attributed to fractional (0.1 e^-) ET to the external circuit coupled to the PT reaction to balance the excess charge induced by deprotonation and maintain a constant electrode potential. Alternatively, when considered as a PT step in the presence of an interfacial electric field, the origin of this slope can be explained by the stabilization of the negatively charged COO⁻ site by the interfacial electric field. Due to dielectric screening by the SAM layer, only ∼ 10% of the total change in electrode potential occurs at the COO⁻ site. These two explanations were shown to be equivalent.[58]

According to eq 2, the grand potential change for the I-PCET reaction at a given electrode potential E is
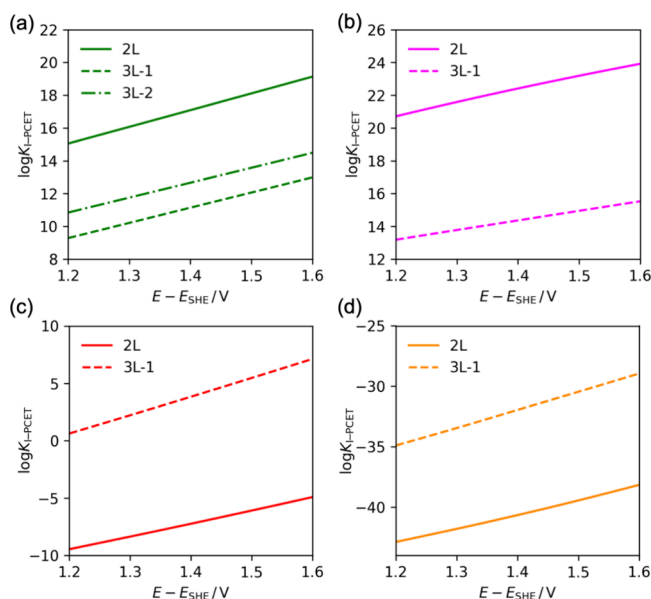

Figure 7. $\log K_{\text{I-PCET}}$ vs E for each I-PCET process in Figure 3 using the same a−d labels for the corresponding processes. Here $\log K_{\text{I-PCET}}$ $= -\Delta\Omega/2.303 k_{\text{B}}T$ and $\Delta\Omega(E) = \Omega_{\text{P}}(E) - \Omega_{\text{R}}(E)$. The corresponding inverse slopes for the 2L and 3L-1 models are given in Table 1. Due to computational expense, we only performed these calculations with the 3L-2 model for case a.

demonstrate nearly linear relationships between $\Delta\Omega(E)$ and E over the experimental potential range. The calculated slopes of $\log K_{\text{I-PCET}}$ vs E for each process are given in Table 1 for the 2L model. The slopes calculated for all four I-PCET processes using the 2L model are ∼ 0.5−0.7-fold smaller than the Nernstian slope for 1H⁺-1e^- PCET (1/59 mV⁻¹) and are consistent with the experimental observations for the Ti/TiO$_y$H$_x$ catalyst (1/107 mV⁻¹), despite the significant differences in the proton-coupled redox potentials. We further find that these slopes depend quantitatively on the thickness of

$$\Delta\Omega(E) = G_{\text{P}}(q_{\text{p}}) - G_{\text{R}}(q_{\text{R}}) - \left(\Delta N_{\text{H}^+} - \frac{\Delta q}{e}\right)\tilde{\mu}_{e^-} \quad (5)$$

where q_R and q_P are the net charge on the reactant and product surfaces, respectively, associated with E. In this expression, $\Delta q = q_P - q_R$, ΔN_{H^+} is the number of protons transferred during the reaction, and $\Delta N_{e^-} = \Delta N_{H^+} - \Delta q/e$ is the number of electrons transferred during the reaction. Therefore, for every proton transferred from the surface, $n = \Delta N_{e^-}/\Delta N_{H^+}$ electrons are removed from the system. This n value is the calculated electrosorption valency of the process. For a $1H^+$-ne^- PCET process, the inverse of the slope $d \log K_{I\text{-PCET}}/dE$ is $59/n$ mV. The calculated values of the electrosorption valencies n for the Au-TiO$_2$ system at $E = 1.4$ V vs SHE in acetonitrile using the three composite models are given in Table 2. The inverse slopes estimated by $59/n$ mV (last row of Table 2) agree well with the calculated values shown in the first row of Table 2.

Table 2. Slope of $\log K_{I\text{-PCET}}$ $(-\Delta\Omega/2.303 k_B T)$ vs. the Electrode Potential Calculated Using Various Models

model	2L	3L-1	3L-2
1/slope (mV)[a]	98	108	110
n[b]	0.55	0.55	0.56
1/est. slope (mV)[c]	106	108	106

[a]Obtained directly from the potential-dependent grand potential calculation at 298 K (Figure 7a). [b]$n = \Delta N_{e^-}/\Delta N_{H^+}$ is the number of electrons transferred from the system when one proton is removed from the surface at $E = 1.4$ V vs SHE in acetonitrile. [c]1/slope estimated as $59/n$ mV.

To understand the electrostatic contribution to the potential dependence of $K_{I\text{-PCET}}(E)$, we quantified the electrostatic potential profile across the Au-TiO$_2$ and Au-TiO$_2$-H systems. Figure 8a,b shows the change in the ESP along the z-axis (perpendicular to the surface) in the Au-TiO$_2$ and Au-TiO$_2$-H systems when the electrode potential changes by 0.1 V, as calculated using the 2L and 3L-2 models, respectively. In the Au slab (10 Å < z < 15 Å), $\Delta\Phi(z)$ does not depend on z, as expected for a metallic system.[19] In the TiO$_2$ slab (17 Å < z <

24 Å for the 2L model and 17 Å < z < 28 Å for the 3L-2 model) and solvent (z > 24 Å for the 2L model and z > 28 Å for the 3L-2 model), the magnitude of $\Delta\Phi(z)$ decreases and eventually drops to zero. For the system with two layers of TiO$_2$, ~ 78% of the total ESP drop occurs in the TiO$_2$ slab, indicating strong dielectric screening by the TiO$_2$ slab. For the system with three layers of TiO$_2$, although the TiO$_2$ slab becomes ~ 1.5 times thicker, the ESP drop in the TiO$_2$ slab is only slightly larger (~84% of the total ESP drop). This finding is consistent with our observation that increasing the thickness by 50% only results in ~ 10% change in the inverse of the slope for the process depicted in Figure 3a (first row in Table 1). Considering only the electrostatic interaction of the charged surface with the ESP, the change of the reaction free energy when the applied potential changes from E_1 to E_2 is

$$\Delta\Delta G_{rxn} = \Delta q (\Phi_{surf}(E_2) - \Phi_{surf}(E_1)) \qquad (6)$$

where Φ_{surf} is the ESP at the interface. According to Figure 8a,b, $\Phi_{surf}(E_2) - \Phi_{surf}(E_1) = 0.22\Delta E$ for the 2L model and $0.16\Delta E$ for the 3L-2 model, averaging the values for both the protonated and deprotonated surfaces, when $\Delta E = E_2 - E_1 = 0.1$ V. The free energy-potential scaling factor $-\Delta\Delta G_{rxn}/|e|\Delta E$ is thus ~ 0.2, assuming $\Delta q = q_P - q_R = -1$ for a deprotonation reaction. This scaling factor leads to a $\log K_{I\text{-PCET}}$ vs E slope of ~ 0.2/59 mV^{-1}, which does not match our calculations for the overall $\log K_{I\text{-PCET}}$ vs E slope.

This lack of quantitative correlation between the ESP drop and the slope could possibly be due to the delocalization of the excess negative charge arising from deprotonation over the TiO$_2$ slabs. Such delocalization contrasts with previous literature studying I-PCET of carboxylic acid groups on SAM interfaces, as the negative charge arising from deprotonation of these carboxylic acids is localized on the COO$^-$ group. To qualitatively illustrate how excess negative charge is distributed in the Au-TiO$_2$ system after deprotonation, we calculated the change in the electron density along the z-axis after removing a proton from the Au-TiO$_2$-H system with a fixed geometry and
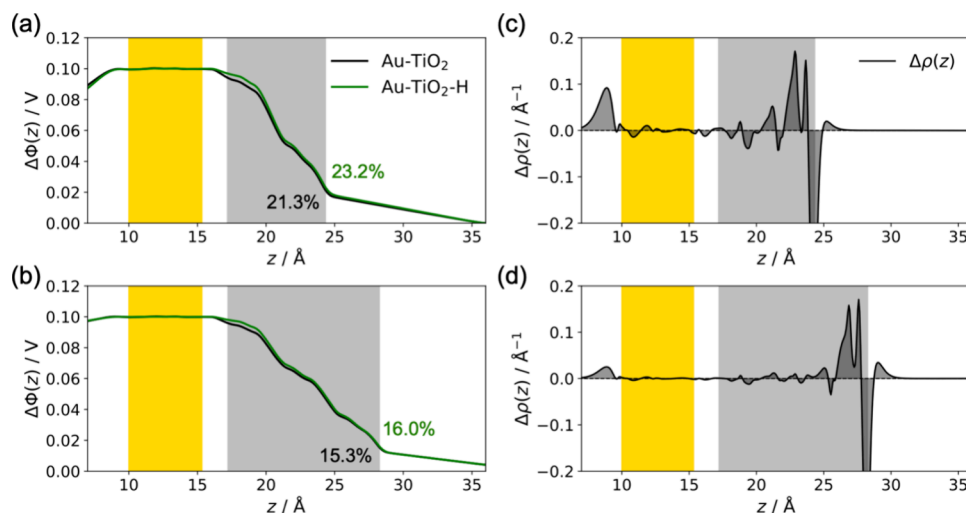

Figure 8. (a, b) Change in the ESP along the z-axis (perpendicular to the surface) for the Au-TiO$_2$ and Au-TiO$_2$-H systems associated with an electrode potential difference of 0.1 V in acetonitrile calculated using the (a) 2L model and (b) 3L-2 model, respectively. Here $\Delta\Phi(z)$ is calculated by subtracting the ESP at $E = 1.3$ V from the ESP at $E = 1.4$ V. The percentages of ESP at the TiO$_2$/solution interface relative to the value of 0.1 V in the Au slab are labeled in black and green for the deprotonated and protonated surfaces, respectively. (c, d) Change in the electron density along the z-axis after removing a proton from the Au-TiO$_2$-H system with a fixed total number of electrons, which corresponds to a system charge $q = +3.82$ and $+3.05$ for the Au-TiO$_2$-H system using the (c) 2L model and (d) 3L-2 model, respectively. In all four panels, the Au slab is indicated by the gold shaded area, and the TiO$_2$ slab is indicated by the gray shaded area.

fixed total number of electrons, as shown in Figure 8c,d for the 2L and 3L-2 models, respectively. Although the number of electrons remains the same after removing the proton, the electrons have clearly redistributed, as evident from the multiple positive and negative peaks in Figure 8c,d. Specifically, the peaks at ∼ 23 and ∼ 24 Å in Figure 8c and the peaks at ∼ 27 and ∼ 28 Å in Figure 8d indicate that some of the negative charge spreads from the deprotonation site to below the surface of the TiO$_2$ slab. However, the mean position of the redistributed electronic charge is only ∼ 1 Å below the surface, where the ESP is still insufficient to cause the observed slope.

To capture the influence of this electron redistribution to the overall $\log K_{\text{I-PCET}}$ vs E scaling, we calculated the differences in capacitive contributions of the EDL between the Au-TiO$_2$ and Au-TiO$_2$-H interfaces to the total free energy of the system. The applied potential influences the total free energy of the interfacial system not only through the electrostatic interaction of the charged surfaces with the ESP, which was discussed above, but also through the energy needed to charge the EDL, which can be expressed as

$$W_{\text{C,R/P}}(E) = \int_{E_{\text{PZFC,R/P}}}^{E} q_{\text{R/P}}(E) \, dE$$
$$\approx \frac{1}{2} C_{\text{R/P}} (E - E_{\text{PZFC,R/P}})^2 \quad (7)$$

where C is the EDL capacitance. Note that both the EDL capacitance and the PZFC can be different for the Au-TiO$_2$ and Au-TiO$_2$-H interfaces. Considering both the electrostatic and capacitive contributions, the change in the reaction free energy when the applied potential changes from E_1 to E_2 is

$$\Delta\Delta G'_{\text{rxn}} = \Delta q (\Phi_{\text{surf}}(E_2) - \Phi_{\text{surf}}(E_1)) + \Delta\Delta W_c \quad (8)$$

where

$$\Delta\Delta W_c = (W_{\text{C,P}}(E_2) - W_{\text{C,P}}(E_1))$$
$$- (W_{\text{C,R}}(E_2) - W_{\text{C,R}}(E_1)) \quad (9)$$

The charge-potential (q-E) relation obtained from the grand potential calculations using the 2L, 3L-1, and 3L-2 models is shown in Figure S7. The slope of the q-E curve gives the differential capacitance C of the surface, and the values for the reactant and the product calculated at $E = 1.4$ V vs SHE are given in Table S5. The capacitance of the Au-TiO$_2$-H system is slightly higher than that of the Au-TiO$_2$ system, and the capacitance decreases as the thickness of the TiO$_2$ slab increases. The calculated $\Delta\Delta W_C$ and $\Delta\Delta G'_{\text{rxn}}$ values using eqs 7– 9 when the applied potential changes from 1.3 to 1.4 V vs SHE are given in Table 3. For the 2L model, when the

Table 3. Calculated $\Delta\Delta W_C$, $\Delta\Delta G'_{rxn}$, and Estimated Slope of $\log K$ vs. the Electrode Potential Calculated Using Various Models

model	2L	3L-1	3L-2
1/slope (mV)[a]	98	108	110
$\Delta\Delta W_C$ (eV)	−0.044	−0.045	−0.045
$\Delta\Delta G'_{rxn}$ (eV)	−0.066	−0.057	−0.061
δ[b]	0.66	0.57	0.61
1/est. slope (mV)[c]	90	103	98

[a]Obtained directly from the potential-dependent grand potential calculation at 298 K (Figure 7a). [b]$\delta = - \Delta\Delta G'_{rxn}/|e|\Delta E$ using eq 8). [c]1/slope estimated as $59/\delta$ mV.

electrode potential increases by 0.1 V, the electrostatic interaction of the charged species with the ESP stabilizes the product by 0.022 eV. Moreover, due to the slightly higher capacitance and more negative PZFC (Tables S5 and S6), charging the EDL requires more energy for the reactant state, which further stabilizes the product by 0.044 eV. However, this effect may depend on the size of the model system. In total, this 0.1 V of potential increase causes a decrease of $\Delta\Delta G'_{\text{rxn}}$ by 0.066 eV. The free energy-potential scaling factor $\delta = -\Delta\Delta G'_{\text{rxn}}/|e|\Delta E$ is thus 0.66, which leads to a $\log K_{\text{I-PCET}}$ vs E slope of 1/90 mV^{-1}. This value agrees well with the grand potential calculation result shown in Table 2 and given again in the first row of Table 3. The same level of agreement is also observed for the 3L-1 and 3L-2 models. Therefore, we conclude that although the electrostatic contribution only leads to a ∼ 0.2 eV decrease of reaction free energy per 1 V potential increase, differences in the capacitive contribution of the protonated and deprotonated surfaces augment this effect to yield a 0.66 eV decrease in the reaction free energy per 1 V change in the applied potential, leading to the observed slope.

■ CONCLUSION

In this paper, we investigated the electronic structure of the Au-TiO$_2$-solution composite system and calculated the potential-dependent grand potential change associated with electrochemical I-PCET for PT from the Au-TiO$_2$ surface to an alcohol acceptor. We determined the proton-coupled redox potential and the I-PCET equilibrium constant-potential scaling for four possible mechanisms that could occur in the system. The calculated slope of the I-PCET equilibrium constant as a function of E for some of the mechanisms agrees well with experimental measurements showing an attenuated potential dependence relative to the metal-solution interface. However, the dependence of the calculated $E_{\text{I-PCET}}$ and slope on the thickness of the TiO$_2$ slab and the use of Au rather Ti for the metal slab prevents a definitive identification of the I-PCET mechanism.

Further analysis of this I-PCET process provides insights into the fundamental physical principles leading to the attenuated potential dependence. Analysis of the surface charge of the reactant and product for a representative I-PCET reaction indicates that each PT from the surface is coupled to the transfer of $n \approx 0.5$ electrons from the metal to the external circuit, and the calculated slope of the grand potential change $\Delta\Omega(E)$ vs E agrees well with the Nernstian slope of a 1H$^+$-ne^- PCET process. Analysis of the electrostatic and capacitive contributions to the system for the same I-PCET mechanism reveals that the electrostatic potential drop in the TiO$_2$ slab would only lead to a ∼ 0.2 eV decrease of the reaction free energy per 1 V potential increase, but the capacitive contribution augments this effect to yield a ∼ 0.6 eV decrease in the reaction free energy per 1 V change in the applied potential, resulting in the observed slope. The electrostatic contribution arises from the potential drop across the titania dielectric, whereas the capacitive contribution arises from differences in how the charge is stored in the EDL when the surface is protonated or deprotonated. This conclusion is expected to hold for other metal−semiconductor systems, including the Ti-TiO$_2$ system, although the quantitative results will be system dependent.

Based on this analysis, tuning reactivity requires consideration of the properties of both the semiconductor layer and the EDL. This study provides key insights into interfacial

PCET processes at electrified metal−semiconductor−solution interfaces by connecting experimentally observed rate-potential scalings to the material properties of the interface. These insights not only enable more precise control of PCET reactivity in these materials but also inform future polarized Brønsted acid catalyst design.

■ ASSOCIATED CONTENT

Data Availability Statement

The data that support the findings of this study are openly available on Zenodo at http://doi.org/10.5281/zenodo.17794830.

Ⓢ Supporting Information

The Supporting Information is available free of charge at https://pubs.acs.org/doi/10.1021/acscatal.5c06789.

> Detailed description of the computational methods; additional constant potential calculation results for defect free and defective Au-TiO$_2$ systems using various models; analysis of the capacitive contribution. (PDF)

■ AUTHOR INFORMATION

Corresponding Author

Sharon Hammes-Schiffer − *Department of Chemistry, Princeton University, Princeton, New Jersey 08544, United States;* ⓞ orcid.org/0000-0002-3782-6995; Email: shs566@princeton.edu

Authors

Kai Cui − *Department of Chemistry, Princeton University, Princeton, New Jersey 08544, United States;* ⓞ orcid.org/0000-0001-7311-1447

Karl S. Westendorff − *Department of Chemical Engineering, Massachusetts Institute of Technology, Cambridge, Massachusetts 02139, United States*

Yuriy Román-Leshkov − *Department of Chemical Engineering, Massachusetts Institute of Technology, Cambridge, Massachusetts 02139, United States;* ⓞ orcid.org/0000-0002-0025-4233

Yogesh Surendranath − *Department of Chemical Engineering and Department of Chemistry, Massachusetts Institute of Technology, Cambridge, Massachusetts 02139, United States;* ⓞ orcid.org/0000-0003-1016-3420

Complete contact information is available at:
https://pubs.acs.org/10.1021/acscatal.5c06789

Notes

The authors declare no competing financial interest.

■ ACKNOWLEDGMENTS

■ REFERENCES

(1) Braunchweig, B.; Hibbitts, D.; Neurock, M.; Wieckowski, A. Electrocatalysis: A Direct Alcohol Fuel Cell and Surface Science Perspective. *Catal. Today* **2013**, *202*, 197−209.

(2) Fried, S. D.; Bagchi, S.; Boxer, S. G. Extreme Electric Fields Power Catalysis in the Active Site of Ketosteroid Isomerase. *Science* **2014**, *346*, 1510−1514.

(3) Chen, L. D.; Urushihara, M.; Chan, K.; Nørskov, J. K. Electric Field Effects in Electrochemical CO$_2$ Reduction. *ACS Catal.* **2016**, *6*, 7133−7139.

(4) Fried, S. D.; Boxer, S. G. Electric Fields and Enzyme Catalysis. *Annu. Rev. Biochem.* **2017**, *86*, 387−415.

(5) Warburton, R. E.; Hutchison, P.; Jackson, M. N.; Pegis, M. L.; Surendranath, Y.; Hammes-Schiffer, S. Interfacial Field-Driven Proton-Coupled Electron Transfer at Graphite-Conjugated Organic Acids. *J. Am. Chem. Soc.* **2020**, *142*, 20855−20864.

(6) Leonard, N. G.; Dhaoui, R.; Chantarojsiri, T.; Yang, J. Y. Electric Fields in Catalysis: From Enzymes to Molecular Catalysts. *ACS Catal.* **2021**, *11*, 10923−10932.

(7) Alvarez-Hernandez, J. L.; Zhang, X.; Cui, K.; Deziel, A. P.; Hammes-Schiffer, S.; Hazari, N.; Piekut, N.; Zhong, M. Long-Range Electrostatic Effects from Intramolecular Lewis Acid Binding Influence the Redox Properties of Cobalt−Porphyrin Complexes. *Chem. Sci.* **2024**, *15*, 6800−6815.

(8) Westendorff, K. S.; Hulsey, M. J.; Wesley, T. S.; Roman-Leshkov, Y.; Surendranath, Y. Electrically Driven Proton Transfer Promotes Brønsted Acid Catalysis by Orders of Magnitude. *Science* **2024**, *383*, 757−763.

(9) Dogonadze, R. R.; Kuznetsov, A. M.; Levich, V. G. Theory of Hydrogen-Ion Discharge on Metals - Case of High Overvoltages. *Electrochim. Acta* **1968**, *13*, 1025.

(10) Ovchinnikov, A. A.; Benderskii, V. A. Theory of Electrochemical Hydrogen Evolution Reactions 0.1. Model and Fundamental Relationships. *J. Electroanal. Chem.* **1979**, *100*, 563−582.

(11) Santos, E.; Lundin, A.; Pötting, K.; Quaino, P.; Schmickler, W. Model for the Electrocatalysis of Hydrogen Evolution. *Phys. Rev. B* **2009**, *79*, No. 235436.

(12) Kastlunger, G.; Lindgren, P.; Peterson, A. A. Controlled-Potential Simulation of Elementary Electrochemical Reactions: Proton Discharge on Metal Surfaces. *J. Phys. Chem. C* **2018**, *122*, 12771−12781.

(13) Goldsmith, Z. K.; Lam, Y. C.; Soudackov, A. V.; Hammes-Schiffer, S. Proton Discharge on a Gold Electrode from Triethylammonium in Acetonitrile: Theoretical Modeling of Potential-Dependent Kinetic Isotope Effects. *J. Am. Chem. Soc.* **2019**, *141*, 1084−1090.

(14) Lamoureux, P. S.; Singh, A. R.; Chan, K. R. pH Effects on Hydrogen Evolution and Oxidation over Pt(111): Insights from First-Principles. *ACS Catal.* **2019**, *9*, 6194−6201.

(15) Lam, Y. C.; Soudackov, A. V.; Goldsmith, Z. K.; Hammes-Schiffer, S. Theory of Proton Discharge on Metal Electrodes: Electronically Adiabatic Model. *J. Phys. Chem. C* **2019**, *123*, 12335−12345.

(16) Lam, Y. C.; Soudackov, A. V.; Hammes-Schiffer, S. Theory of Electrochemical Proton-Coupled Electron Transfer in Diabatic Vibronic Representation: Application to Proton Discharge on Metal Electrodes in Alkaline Solution. *J. Phys. Chem. C* **2020**, *124*, 27309−27322.

(17) Warburton, R. E.; Soudackov, A. V.; Hammes-Schiffer, S. Theoretical Modeling of Electrochemical Proton-Coupled Electron Transfer. *Chem. Rev.* **2022**, *122*, 10599−10650.

(18) Chen, X.; Kastlunger, G.; Peterson, A. A. Fundamental Drivers of Electrochemical Barriers. *Phys. Rev. Lett.* **2023**, *131*, No. 238003.

(19) Schmickler, W.; Santos, E. *Interfacial Electrochemistry, Second ed.*; Springer, 2010.

(20) Zhang, Z.; Yates, J. T., Jr. Band Bending in Semiconductors: Chemical and Physical Consequences at Surfaces and Interfaces. *Chem. Rev.* **2012**, *112*, 5520−5551.

(21) Khomyakov, P. A.; Giovannetti, G.; Rusu, P. C.; Brocks, G.; van den Brink, J.; Kelly, P. J. First-Principles Study of the Interaction and Charge Transfer between Graphene and Metals. *Phys. Rev. B* **2009**, *79*, No. 195425.

(22) Campbell, Q.; Dabo, I. Quantum-Continuum Calculation of the Surface States and Electrical Response of Silicon in Solution. *Phys. Rev. B* **2017**, *96*, No. 039901.

(23) Wang, Q.; Shao, Y.; Shi, X. Mechanism of Charge Redistribution at the Metal-Semiconductor and Semiconductor-Semiconductor Interfaces of Metal-Bilayer MoS_2 Junctions. *J. Chem. Phys.* **2020**, *152*, No. 244701.

(24) Gong, C.; Colombo, L.; Wallace, R. M.; Cho, K. The Unusual Mechanism of Partial Fermi Level Pinning at Metal-MoS_2 Interfaces. *Nano Lett.* **2014**, *14*, 1714−1720.

(25) Sajjad, M.; Yang, X.; Altermatt, P.; Singh, N.; Schwingenschlögl, U.; De Wolf, S. Metal-Induced Gap States in Passivating Metal/Silicon Contacts. *Appl. Phys. Lett.* **2019**, *114*, No. 071601.

(26) Zur, A.; Mcgill, T. C.; Smith, D. L. Fermi-Level Position at a Semiconductor-Metal Interface. *Phys. Rev. B* **1983**, *28*, 2060−2067.

(27) Deskins, N. A.; Rousseau, R.; Dupuis, M. Localized Electronic States from Surface Hydroxyls and Polarons in TiO_2 (110). *J. Phys. Chem. C* **2009**, *113*, 14583−14586.

(28) Jiao, Y.; Hellman, A.; Fang, Y.; Gao, S.; Käll, M. Schottky Barrier Formation and Band Bending Revealed by First-Principles Calculations. *Sci. Rep.* **2015**, *5*, 11374.

(29) Lohaus, C.; Klein, A.; Jaegermann, W. Limitation of Fermi Level Shifts by Polaron Defect States in Hematite Photoelectrodes. *Nat. Commun.* **2018**, *9*, 4309.

(30) Rousseau, R.; Glezakou, V.-A.; Selloni, A. Theoretical Insights into the Surface Physics and Chemistry of Redox-Active Oxides. *Nat. Rev. Mater.* **2020**, *5*, 460−475.

(31) Van de Walle, C. G. Hydrogen as a Cause of Doping in Zinc Oxide. *Phys. Rev. Lett.* **2000**, *85*, 1012−1015.

(32) Paier, J.; Penschke, C.; Sauer, J. Oxygen Defects and Surface Chemistry of Ceria: Quantum Chemical Studies Compared to Experiment. *Chem. Rev.* **2013**, *113*, 3949−3985.

(33) Warburton, R. E.; Mayer, J. M.; Hammes-Schiffer, S. Proton-Coupled Defects Impact O-H Bond Dissociation Free Energies on Metal Oxide Surfaces. *J. Phys. Chem. Lett.* **2021**, *12*, 9761−9767.

(34) Warburton, R. E.; Soudackov, A. V.; Hammes-Schiffer, S. Interfacial Proton-Coupled Electron Transfer via Localized Trap States on Metal Oxide Surfaces. *J. Phys. Chem. C* **2024**, *128*, 7903−7912.

(35) Perdew, J. P.; Burke, K.; Ernzerhof, M. Generalized Gradient Approximation Made Simple. *Phys. Rev. Lett.* **1996**, *77*, 3865−3868.

(36) Anisimov, V. I.; Aryasetiawan, F.; Lichtenstein, A. I. First-Principles Calculations of the Electronic Structure and Spectra of Strongly Correlated Systems: The LDA+U Method. *J. Phys.-Condens. Matter* **1997**, *9*, 767−808.

(37) Giannozzi, P.; Baroni, S.; Bonini, N.; Calandra, M.; Car, R.; Cavazzoni, C.; Ceresoli, D.; Chiarotti, G. L.; Cococcioni, M.; Dabo, I.; et al. QUANTUM ESPRESSO: A Modular and Open-Source Software Project for Quantum Simulations of Materials. *J. Phys.: Condens. Matter* **2009**, *21*, No. 395502.

(38) Giannozzi, P.; Andreussi, O.; Brumme, T.; Bunau, O.; Nardelli, M. B.; Calandra, M.; Car, R.; Cavazzoni, C.; Ceresoli, D.; Cococcioni, M.; et al. Advanced Capabilities for Materials Modelling with Quantum ESPRESSO. *J. Phys.: Condens. Matter* **2017**, *29*, No. 465901.

(39) Perdew, J. P.; Levy, M. Physical Content of the Exact Kohn-Sham Orbital Energies - Band-Gaps and Derivative Discontinuities. *Phys. Rev. Lett.* **1983**, *51*, 1884−1887.

(40) Sham, L. J.; Schluter, M. Density-Functional Theory of the Energy Gap. *Phys. Rev. Lett.* **1983**, *51*, 1888−1891.

(41) Paier, J.; Marsman, M.; Kresse, G. Why Does the B3LYP Hybrid Functional Fail for Metals? *J. Chem. Phys.* **2007**, *127*, No. 024103.

(42) Gao, W.; Abtew, T. A.; Cai, T.; Sun, Y. Y.; Zhang, S.; Zhang, P. On the Applicability of Hybrid Functionals for Predicting Fundamental Properties of Metals. *Solid State Commun.* **2016**, *234-235*, 10−13.

(43) Hu, Z. P.; Metiu, H. Choice of U for DFT plus U Calculations for Titanium Oxides. *J. Phys. Chem. C* **2011**, *115*, 5841−5845.

(44) Thoa, T. T.; Van Hung, H.; Hue, N. T. M. Study on structural and electronic properties of rutile $TiO2$ using DFT + U approach. *Vietnam J. Chem.* **2022**, *60*, 183−189.

(45) Hutchison, P.; Warburton, R. E.; Soudackov, A. V.; Hammes-Schiffer, S. Multicapacitor Approach to Interfacial Proton-Coupled Electron Transfer Thermodynamics at Constant Potential. *J. Phys. Chem. C* **2021**, *125*, 21891−21901.

(46) Chan, K. R.; Norskov, J. K. Electrochemical Barriers Made Simple. *J. Phys. Chem. Lett.* **2015**, *6*, 2663−2668.

(47) Chan, K.; Nørskov, J. K. Potential Dependence of Electro-chemical Barriers from Ab Initio Calculations. *J. Phys. Chem. Lett.* **2016**, *7*, 1686−1690.

(48) Sundararaman, R.; Figueiredo, M. C.; Koper, M. T.; Schwarz, K. A. Electrochemical Capacitance of CO-Terminated Pt (111) Dominated by The CO−Solvent Gap. *J. Phys. Chem. Lett.* **2017**, *8*, 5344−5348.

(49) Gauthier, J. A.; Dickens, C. F.; Heenen, H. H.; Vijay, S.; Ringe, S.; Chan, K. Unified Approach to Implicit and Explicit Solvent Simulations of Electrochemical Reaction Energetics. *J. Chem. Theory Comput.* **2019**, *15*, 6895−6906.

(50) Hörmann, N. G.; Andreussi, O.; Marzari, N. Grand Canonical Simulations of Electrochemical Interfaces in Implicit Solvation Models. *J. Chem. Phys.* **2019**, *150*, No. 041730.

(51) Hörmann, N. G.; Marzari, N.; Reuter, K. Electrosorption at Metal Surfaces from First Principles. *Npj Comput. Mater.* **2020**, *6*, 136.

(52) Groβ, A. Grand-Canonical Approaches to Understand Structures and Processes at Electrochemical Interfaces from an Atomistic Perspective. *Curr. Opin. Electrochem.* **2021**, *27*, No. 100684.

(53) Nørskov, J. K.; Rossmeisl, J.; Logadottir, A.; Lindqvist, L.; Kitchin, J. R.; Bligaard, T.; Jónsson, H. Origin of the Overpotential for Oxygen Reduction at a Fuel-Cell Cathode. *J. Phys. Chem. B* **2004**, *108*, 17886−17892.

(54) Gauthier, J. A.; Dickens, C. F.; Heenen, H. H.; Vijay, S.; Ringe, S.; Chan, K. Unified Approach to Implicit and Explicit Solvent Simulations of Electrochemical Reaction Energetics. *J. Chem. Theory Comput* **2019**, *15*, 6895−6906.

(55) Gauthier, J. A.; Dickens, C. F.; Ringe, S.; Chan, K. Practical Considerations for Continuum Models Applied to Surface Electro-chemistry. *ChemPhysChem* **2019**, *20*, 3074−3080.

(56) Connelly, N. G.; Geiger, W. E. Chemical Redox Agents for Organometallic Chemistry. *Chem. Rev.* **1996**, *96*, 877−910.

(57) Agarwal, R. G.; Coste, S. C.; Groff, B. D.; Heuer, A. M.; Noh, H.; Parada, G. A.; Wise, C. F.; Nichols, E. M.; Warren, J. J.; Mayer, J. M. Free Energies of Proton-Coupled Electron Transfer Reagents and Their Applications. *Chem. Rev.* **2022**, *122*, 1−49.

(58) Ge, A. M.; Kastlunger, G.; Meng, J. H.; Lindgren, P.; Song, J.; Liu, Q. L.; Zaslavsky, A.; Lian, T. Q.; Peterson, A. A. On the Coupling of Electron Transfer to Proton Transfer at Electrified Interfaces. *J. Am. Chem. Soc.* **2020**, *142*, 11829−11834.

(59) Boerner, T. J.; Deems, S.; Furlani, T. R.; Knuth, S. L.; Towns, J. Access: Advancing Innovation: NSF's Advanced Cyberinfrastructure Coordination Ecosystem: Services & Support. In *Practice and experience in advanced research computing 2023: Computing for the common good* 2023; pp 173−176.